

Design and performance prediction of an impedance void meter applied to the petroleum industry

This article has been downloaded from IOPscience. Please scroll down to see the full text article.

2012 Meas. Sci. Technol. 23 055304

(<http://iopscience.iop.org/0957-0233/23/5/055304>)

View [the table of contents for this issue](#), or go to the [journal homepage](#) for more

Download details:

IP Address: 143.106.21.131

The article was downloaded on 17/04/2012 at 14:52

Please note that [terms and conditions apply](#).

Design and performance prediction of an impedance void meter applied to the petroleum industry

E S Rosa, B F Flora and M A S F Souza

Mechanical Engineering Faculty, State University of Campinas, São Paulo, Brazil

E-mail: erosa@fem.unicamp.br

Received 20 December 2011, in final form 27 February 2012

Published 17 April 2012

Online at stacks.iop.org/MST/23/055304

Abstract

A novel methodology based on numerical simulation is developed for designing a gas–liquid void fraction meter operating on the principle of electrical impedance. The numerical simulations employ software based on the finite volume method. The analysis allowed heuristic optimization of the electrodes' geometry and also the establishment of the calibration curve according to the electrical properties of the fluids in question. Using dimensional analysis it is possible to reduce the electrical impedance estimates into simple algebraic expressions relating the void fraction to the dimensionless voltage output. Dynamic tests are performed using air and water in order to validate the computational study and verify the performance of the sensor operating at different flow patterns.

Keywords: impedance probe, void fraction, gas and liquid flow, numerical modeling

(Some figures may appear in colour only in the online journal)

1. Introduction

Production of crude oil occurs along lines which connect the oil reservoir to the oil rig. The mixture of gas and oil is complex not only because of the two-phase nature of the flow but also due to the changes in the gas–liquid phase equilibrium during the mixture transport, the heat transfer phenomena, particularly in subsea lines, and the presence of paraffin or hydrates which may build up along the line, to quote a few. Furthermore, the gas–oil properties may change due to additional causes such as well ageing which often brings water and eventually the formation of water-in-oil emulsion or, for almost depleted reservoirs, oil-in-water emulsions. The simultaneous occurrences of these phenomena add complexity to flow prediction models and challenge production engineers to effectively monitor, control and optimize the oil production. The accomplishment of these tasks ensures a successful and economical flow of hydrocarbon from the reservoir to on-shore or off-shore oil rigs.

The flow assurance is assessed mostly by the use of flow simulators which estimate the flow pattern, the phases' velocities, volumetric concentration, the pressure drop, heat

transfer rate and mixture temperature among other flow properties. The accuracy of these estimates depends on the accuracy of the gas–liquid properties and also on the physical models built-in on the flow simulators. In ordinary oil fields uncertainties arise in the ever changing gas–oil properties due to well ageing. On the other hand, in the development of new fields which operate at extreme conditions inaccuracies may come from the flow simulators. In fact, scenarios with high pressure and temperature may lead to gas–liquid phases with small differences in specific weight, mitigation of surface tension effects or mixtures where one phase is in supercritical state; additionally lines with large diameter are also an uncertainty factor. Quite often there is a lack of knowledge regarding two-phase flow under these conditions.

One way to enhance the accuracy of the flow estimates is by means of acquiring field data and using them as input data to the flow models or also as a way to cross-check them. The motivation of this work is to acquire void fraction data to aid the operations of monitoring, controlling and optimization of crude production. The void fraction, or simply α , is defined by the ratio between the volume occupied by the gas phase and the total volume of the mixture. It is a fundamental quantity

appearing in most of the flow models and frequently applied to assist flow pattern identification routines as well as two-phase flow rate estimates.

The development of a void fraction meter for crude oil production demands several stages of research and field tests. This paper lays out the first stage of development by designing a void fraction meter based on electrical impedance measurement satisfying the following requirements: (a) it has to operate with liquids exhibiting conductive behavior such as water solutions as well as with liquids having dielectric properties such as oils; (b) the electrodes' design has to be able to detect void fraction waves with wavelength of a few pipe diameters, allow a simple mechanical housing and ensure a good shield against external noises; and (c) assessment of the calibration curve has to be performed through numerical simulation of the electrostatic field.

This analysis applies only to vertical two-phase flows. The sensor may handle one gas phase and two liquid phases if the liquid phases are homogeneous. Typically, emulsions of oil in water as well as water in oil fit into this category. The occurrence of three-phase flows, i.e. gas, oil and water phases, even though it is common in crude oil production, is considered out of the scope of this work.

1.1. Void fraction measurement

Hammer *et al* (2006) list several techniques for void fraction measurement; among them they quote: radiation methods, optical sensors, ultrasound and electrical impedance methods. The present work selects the electrical impedance method because it has a relatively simple measuring principle, a reasonable cost, its mechanical parts and driving electronics are suitable for field application and also it is not potentially hazardous to the environment. The method is based on the phase differences in permittivity or conductivity. One recent review on the subject is in Ceccio and George (1996) which describes a variety of techniques including bulk and local void fraction meters, film thickness probes and electrical impedance tomography.

The impedance techniques may be grouped into two categories: capacitive and resistive sensors. Capacitive sensors mostly operate with dielectric liquids. The literature discloses driving circuits with frequencies ranging from 100 kHz to 10 MHz and electrical impedance within 0.1 to 10 M Ω . The electrode surfaces may be in direct contact with the gas–liquid mixture or insulated by a thin dielectric sleeve. Previous works on capacitive sensors with distinct electrode geometry are found in Abouelwafa and Kendall (1980), Elkow and Rezkallah (1996), Ahmed (2006) and Carnière *et al* (2007). The resistive sensors operate with conducting liquids transferring electrical charges from one electrode's surface to the other. The impedance is defined only by its resistance component, which typically ranges from 1 Ω to 100 k Ω . The literature reports oscillator frequencies ranging from 10 to 500 kHz. Resistivity sensors have, necessarily, electrodes in contact with the gas–liquid mixture. The electrode's polarization, also known as the double layer effect, is avoided by selecting exciting frequencies above 100 kHz (Asali *et al*

1985). A few selected works on resistivity sensors exhibiting distinct electrode geometry are found in Andreussi *et al* (1988), Costigan and Whalley (1996), Fossa *et al* (2003) and Rocha and Simões-Moreira (2008).

According to Cimorelli and Evangelisti (1967), capacitance measurement is preferred to resistance measurement because the first is based on the permittivity, ϵ , which is predominantly a function of temperature while the conductivity, σ , is dependent on temperature as well as on the kind and on the ion concentration present in the liquid phase. The capacitance technique may also be applied to conducting liquids if the exciting frequency, ω , is high but its usage introduces sources of electrical instabilities making the electronic circuit very sensitive to stray capacitances and proximity effects. On the other hand, circuit drivers to measure resistivity are simple and reliable but referencing is troublesome because one has to control the fluid temperature and the ion concentration.

This work focuses on void fraction sensors with non-intrusive electrodes because they do not disturb the flow and allow line workover, an important feature of oil field application. A variety of non-intrusive electrode configurations have been designed by a number of researchers, ranging from a pair or multiple concave plates, helical and multiple helical wound electrodes and double rings (Andreussi *et al* 1988, Gregory and Mattar 1973, Merilo *et al* 1977, Sami *et al* 1980, Geraets and Borst 1988).

The geometrical properties of the electrodes define three important characteristics: the spatial resolution, the sensitivity and the linearity. The spatial resolution is directly associated with the electrode axial length; the minimum wavelength of void waves that can be properly detected increases as the electrode axial length increases. Among the electrodes' configurations the helical wound electrode is the bulkiest, demanding an axial length of 6 pipe diameters (Geraets and Borst 1988). The concave plates as well as the pair of rings demand axial lengths ranging, typically, from 1/2 to 2 pipe diameters. The sensitivity is defined as the ratio of the output voltage to the changes in the void fraction, $dV/d\alpha$. The helical wound electrodes have the highest sensitivity for exhibiting the largest electrodes' areas. Trailing the sensitivity of the helical wound electrodes are the ring and the concave electrodes with the ring electrodes having a higher sensitivity than the concave electrodes (Ahmed 2006). The dependence of the void fraction on the output voltage follows, approximately, a linear relationship. The best linearity of $\alpha \times V$ is found for helical electrodes (Gregory and Mattar 1973). The rings and the concave electrodes working in horizontal gas–liquid flows exhibited a near linear behavior as shown in Ahmed (2006), Fossa *et al* (2003) and Lowe and Rezkallah (1999).

The theoretical foundation for the impedance techniques was established by Maxwell (1873) who first proposed a theoretical model based on the electrical impedance to measure small volumetric concentrations of fine solid particles uniformly dispersed in a continuum. For referencing purposes equation (1) displays the permittivity, ϵ_m , and the conductivity, σ_m , of mixtures evaluated by Maxwell theory; the subscripts m , d and c mean the properties belonging to the mixture, dispersed

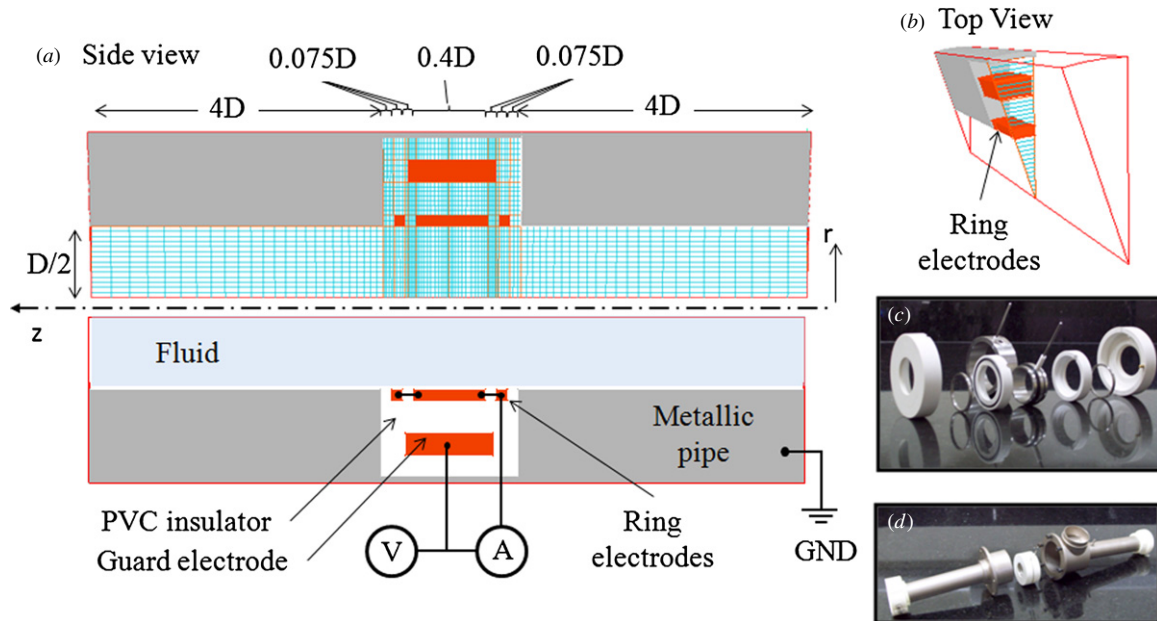


Figure 1. Ring sensor: (a) schematic representation, sizes and numerical grid, (b) top view showing ring and guard electrodes, (c) parts and (d) assembly.

and continuous phases respectively:

$$\varepsilon_m = \varepsilon_c \frac{1 + 2\alpha \left(\frac{\varepsilon_d - \varepsilon_c}{\varepsilon_d + 2\varepsilon_c} \right)}{1 - \alpha \left(\frac{\varepsilon_d - \varepsilon_c}{\varepsilon_d + 2\varepsilon_c} \right)} \quad \text{and} \quad \sigma_m = \sigma_c \frac{1 + 2\alpha \left(\frac{\sigma_d - \sigma_c}{\sigma_d + 2\sigma_c} \right)}{1 - \alpha \left(\frac{\sigma_d - \sigma_c}{\sigma_d + 2\sigma_c} \right)}. \quad (1)$$

The mixture's permittivity or conductivity is a function of the continuous phase property times a correction coefficient which is a function of the volumetric concentration, α ; when $\alpha = 0$ then $\varepsilon_m = \varepsilon_c$ and $\sigma_m = \sigma_c$. Nearly a century after the pioneering work of Maxwell, theoretical and numerical models started to be developed to establish design criteria for the impedance sensors. A theoretical model for ring electrodes was first proposed by Andreussi *et al* (1988) based on the work of Coney (1973) on strip electrodes. Tsochatzidis *et al* (1992) proposed an analytical solution to the ring probe by solving the Laplace equation in cylindrical coordinates. Geraets and Borst (1988) reduced the helical wound electrode to an axially symmetrical setup and, using a polar coordinate system, obtained an analytical solution based on Fourier series expansion for annular and disperse flows. Ahmed (2006) proposed theoretical models for ring and concave electrodes based on equivalent capacitor models. Ahmed's models agree within 15% with the experimental data. A two-dimensional numerical solution of the electrostatic field for concave plate electrodes was obtained by Costigan and Whalley (1996) using finite volume code and also by Carnière *et al* (2007) employing a finite element code.

2. Design considerations

The development of a void meter applied to the oil industry has several operational constraints which have to be satisfied. This section addresses some of these constraints which define the sensor design. Non-intrusiveness is a necessary characteristic of the electrodes which allows the insertion of tools inside the

line for maintenance and diagnosis purposes. Another aspect to be considered is the fact that the impedance meter has to work at two extremes characterized by flows with gas–oil and gas–water mixtures which have capacitive and resistive behaviors, respectively. This requirement has implications for the driving circuit and the electrodes which are dealt with by choosing a driving circuit operating above 100 kHz with electrodes in contact with the gas–liquid mixture. This choice is based on the fact that Cimorelli and Evangelisti (1967) claimed that the advantage of the capacitive methods over the resistive ones is not true for this application. Actually the permittivity of a hydrocarbon mixture is dependent on two variables: the temperature and the concentration of the dissolved gas in the liquid phase due to the high solubility of the gas phase in hydrocarbon mixtures. Furthermore, exciting frequencies above 100 kHz avoid the double layer capacitive effect on the electrodes for conducting liquids. The choices of non-intrusive electrodes reduce to three geometries: helical wound electrodes, concave plates and rings. The first is not considered an option because it is bulky with complex mechanical parts and has low spatial resolution. The concave and ring electrodes are not bulky, have equivalent spatial resolution and linearity but the ring electrodes have a better sensitivity than the concave plates (Ahmed 2006). Based on these facts the rings are selected as the working electrode geometry.

The sensor is schematically represented in figure 1. The figure shows the sensor components, the rings and guard electrodes, the electrical insulator, the pipe housing, the main axial dimensions, the assembly, the wire connections and the numerical grid. The configuration employed has the center electrode adjacent to two border electrodes flush with the inner pipe wall. The three rings are flush to the inner pipe wall and are at the same potential; the fourth electrode is the pipe wall itself which, in its turn, is at ground potential. Choosing the pipe wall as a receiving electrode is convenient because it provides

simultaneously a shield against external noise (electrostatic and electromagnetic fields) and also mechanical protection to the rings. The ring electrodes are made of stainless steel 316 with an insulating housing made of PVC assembled in a steel pipe. A series of numerical simulations were performed to improve, heuristically, the electrode sensitivity to impedance changes at the pipe core as well as near the wall. The optimum axial lengths for the central and border electrodes as well as for the electrical insulation are $0.4D$, $0.075D$ and $0.075D$, respectively; the setup has a total axial length of $0.85D$. To minimize stray impedance a guard electrode is added to guide the electric field lines to cross the two-phase mixture flowing inside the pipe. A simple electronic schematic is also shown in the figure having the voltage source V connecting the guard and ring electrodes but the ammeter A measuring the current drawn by the ring electrodes only. Further details on the electronics are in section 4.1 and the numerical grid is fully presented in section 3.2. They were displayed all together in this figure for the sake of conciseness.

The following sections address impedance modeling, experimental measurements and comparison among the predicted and measured quantities.

3. Modeling the impedance across the electrodes

The phases may exhibit a capacitive or resistive behavior. The gas phase is a dielectric medium; therefore its impedance reduces to the capacitive component, C_g . The liquid phase may exhibit dominance of a dielectric or of a conductive behavior. Oil and non-polar liquids have, in general, the impedance represented by the capacitive component, C_l , and complementary to it, water solutions have their impedance represented only by the resistive component, R_l . The dominance of the capacitive or the resistive components is estimated by employing the ratio $(\omega\epsilon/\sigma)^2$; when this ratio is much greater than 1 or much smaller than 1 the liquid impedance is represented by its capacitive or resistive component, respectively. Emulsions of water in oil (W-O) or oil in water (O-W) are a special case because these are two immiscible liquid phases. Considering the emulsions as a homogeneous mixture, their permittivity and conductivity can be evaluated by Maxwell theory for composite media, see equation (1), or else by more accurate models, see Sowa *et al* (1995). As an example consider a scenario where oil and water have relative permittivity and conductivity constants of (2, 80) and $(10^{-12}, 5) \text{ S m}^{-1}$, respectively, and an electronic circuit with exciting frequency of 1 MHz. By using equation (1) it is possible to estimate ϵ_m and σ_m for (W-O) and (O-W) and evaluate the dimensionless ratio $(\omega\epsilon_m/\sigma_m)^2$ and find that this ratio is much greater than 1 for (W-O) or much lower than 1 for (O-W). This indicates that (W-O) has a capacitive behavior while (O-W) has a resistive behavior. Summarizing, liquids, as a single-phase fluid or constituted by an emulsion, are characterized as showing either capacitive or resistive behavior.

The equivalent capacitance and the resistance of the gas-liquid mixture are defined in equation (2) in terms of

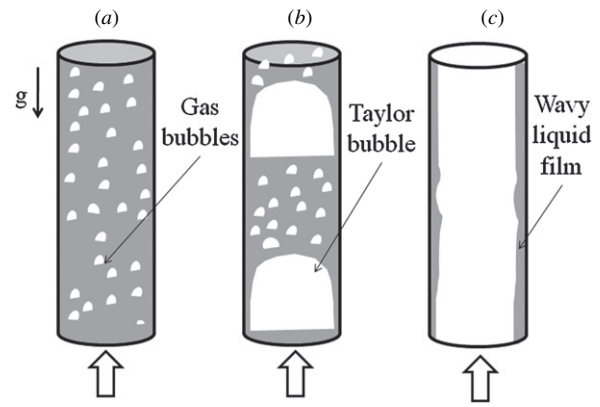


Figure 2. Flow patterns' representation for vertical flow: (a) bubbly, (b) intermittent and (c) separated.

the voltage difference between electrodes, ΔV , the polarized charges, Q , and the electrical current, I :

$$C = \frac{Q}{\Delta V} = \frac{\oint_S \epsilon (\nabla V \cdot \mathbf{n}) dA}{\Delta V} \quad \text{and} \quad R = \frac{\Delta V}{I} = \frac{\Delta V}{\oint_S \sigma (\nabla V \cdot \mathbf{n}) dA}. \quad (2)$$

For numerical evaluation purposes C and R are also expressed in equation (2) by the flux of the electrical field, $\mathbf{E} = -\nabla V$ at S , a surface coincident with the ring area. When the volume comprised by the electrodes is filled with a homogeneous fluid the product CR is equal to the ratio between the permittivity and the conductivity, i.e. $CR = \epsilon/\sigma$.

For an application scenario where $\omega D/c \ll 1$, D being the pipe diameter and c the speed of light, the electrical phenomenon changes at a rate much slower than the signal velocity, allowing the phenomenon to be modeled as an electrostatic field (Haus *et al* 1989). Under the electro-quasi-static framework the sensor's electric potential satisfies the Laplace equation defined in equation (3) for dielectric and conductive media:

$$\nabla \cdot (\epsilon \nabla V) = 0 \quad \text{and} \quad \nabla \cdot (\sigma \nabla V) = 0, \quad (3)$$

where the permittivity and the conductivity may change in space accordingly to the phases' spatial distribution, i.e. $\epsilon = \epsilon(\mathbf{r})$ and $\sigma = \sigma(\mathbf{r})$.

3.1. Phases' spatial distribution

Modeling the spatial distribution of ϵ and σ due to the gas-liquid content requires first the knowledge on how the phases are distributed inside the pipe. The simplest classification of the phases' spatial distribution into upward concurrent vertical flows employs three flow pattern descriptors: the bubbly flow, the separated flow and the intermittent flow (Brennen 2005). The bubbly flow has the gas phase spatially distributed in the form of bubbles, see the schematic representation in figure 2(a). The separated flow has the gas and liquid phases flowing concurrently but separated by an interface, better known as annular flows, see figure 2(c). The intermittent pattern is described as a succession of aerated liquid pistons trailed by elongated gas bubbles surrounded by an annular liquid film

known as slug flows. For modeling purposes the intermittent pattern is considered as an alternate combination of bubbly and separated flows, see figure 2(b).

3.1.1. The bubbly flow. For impedance modeling purposes the bubbles have spherical shapes and are distributed non-uniformly on the pipe cross section. The radial void profile may exhibit a peak either near the wall or at the pipe centerline (Serizawa *et al* 1975, Liu 1993, Hibiki and Ishii 2002). The void radial profile evolves from a wall-peak to core-peak trend with an increase in the gas input or also when the bubble size increases (Liu 1993, Guet and Ooms 2006). An appraisal on the flow map areas where void profiles have a core-peak and a wall-peak is given in Hibiki and Ishii (2002). This work employs a core-peak radial void profile as defined in equation (4) to consider it more typical to the void meter's application scenario:

$$\frac{\alpha(r/R)}{\langle \alpha \rangle} = \frac{n+2}{n} \left[1 - \left(\frac{r}{R} \right)^n \right], \quad (4)$$

where r , R , n and $\langle \alpha \rangle$ are, respectively, the radial coordinate, the pipe radius, the power coefficient and the cross section averaged void fraction. This profile has a null void fraction at the wall and applies to adiabatic flow, i.e. no boiling. A linear profile occurs when $n = 1$; it is not likely to happen in actual cases; nevertheless $n = 1$ is considered as a lower bound. As n increases, the tendency is to lower the maximum void fraction; for large n the profile approaches asymptotically the shape of a flat profile.

The gas bubbles affect the electrical field resulting in an impedance change. There are at least two possibilities to numerically estimate the impedance changes: one is the insertion of spherical voids along the numerical domain according to equation (4) and the other is to treat the gas-liquid as a mixture with equivalent permittivity and conductivity changing continuously along the radial direction. The first approach has the phases' electrical properties (dielectric or conductivity) spatially distributed along the domain in stepwise changes corresponding to the voids. To achieve numerical accuracy the grid size has to be large enough to resolve a single bubble. For example consider that 10 cells along each direction are enough to properly resolve a single spherical bubble on the electrical field. Furthermore, assuming that the bubbles' diameters are in a scale of 1:10 to the pipe diameter, one obtains grid sizes with at least 10^6 cells. This approach is not considered a feasible option due to the large computer power demanded. The second option resorts to the Maxwell model which is correct if the bubbles are uniformly distributed along the pipe cross section. Under the premise that the void spatial distribution is stationary, at least on the sensor measurement volume, it is postulated that the Maxwell model is valid locally, i.e. the local mixture properties, ε_m or σ_m , depend on the local void fraction following the Maxwell model:

$$\frac{\varepsilon_m(r/R)}{\varepsilon_l} = \frac{1 + 2\alpha(r/R) \left(\frac{\varepsilon_g - \varepsilon_l}{\varepsilon_g + 2\varepsilon_l} \right)}{1 - \alpha(r/R) \left(\frac{\varepsilon_g - \varepsilon_l}{\varepsilon_g + 2\varepsilon_l} \right)} \quad \text{and} \quad \frac{\sigma_m(r/R)}{\sigma_l} = \frac{1 - \alpha(r/R)}{1 + \frac{1}{2}\alpha(r/R)}, \quad (5)$$

where $\alpha(r/R)$ is given according to equation (4). For void fraction values lower than 0.2, typical for bubbly flow, equation (5) is further simplified by a first-order expansion. Furthermore, substituting the radial void profiles one obtains approximate expressions for the local mixture properties ε_m or σ_m :

$$\begin{aligned} \frac{\varepsilon_m(r/R)}{\varepsilon_l} &\cong 1 + 3\langle \alpha \rangle \left(\frac{n+2}{n} \right) \left[1 - \left(\frac{r}{R} \right)^n \right] \left(\frac{\varepsilon_g - \varepsilon_l}{\varepsilon_g + 2\varepsilon_l} \right) \\ \frac{\sigma_m(r/R)}{\sigma_l} &\cong 1 - \frac{3}{2}\langle \alpha \rangle \left(\frac{n+2}{n} \right) \left[1 - \left(\frac{r}{R} \right)^n \right]. \end{aligned} \quad (6)$$

Equation (6) enables us to estimate ε_m and σ_m as a function of the radial position. The liquid phase is always in contact with the wall; therefore for $r = R$ one obtains $\varepsilon_m(1) = \varepsilon_l$ or $\sigma_m(1) = \sigma_l$. At the pipe core, $r = 0$, the dielectric or conductivity of the mixture changes by a factor dependent on the cross section void fraction and on n .

3.1.2. The annular flow. For impedance modeling purposes the annular flow is considered to have a smooth interface dividing the gas core from the liquid film. The electrical properties of the gas core and the liquid film are represented by the gas permittivity constant, ε_g , and by the liquid phase electrical property, ε_l or σ_l . The gas core permittivity does not consider the effect of entrained liquid droplets. Similarly, the liquid film does not consider the presence of gas bubbles or its rough interface. The cross section void fraction is expressed through the ratio between the film thicknesses and the pipe radius: $\langle \alpha \rangle = 2(\delta/R)(1 - \delta/R)$ and the associated electrical properties are defined as

$$\begin{aligned} \text{then } \varepsilon_m \left(\frac{r}{R} \right) &= \varepsilon_g \text{ or } \sigma_m \left(\frac{r}{R} \right) = \sigma_g \\ \text{if } r/R \leq 1 - \delta/R & \\ \text{else } \varepsilon_m \left(\frac{r}{R} \right) &= \varepsilon_l \text{ or } \sigma_m \left(\frac{r}{R} \right) = \sigma_l \end{aligned} \quad (7)$$

A mathematical model similar to the one described above was proposed by Kim *et al* (2010).

3.2. Numerical method

The electric potential V is determined by solving equation (3) numerically employing either the permittivity or the conductivity depending on whether the liquid phase exhibits capacitive or resistive behavior. The numerical estimates of V come from a finite volume code built-in on the Phoenix[®], a commercial software package. An axis-symmetric polar coordinate system (r , z) is chosen to fit the domain since the void distribution is azimuthally symmetric. The computational domain along the radial, axial and tangential directions is $1D$, $5D$ and 1 radian, respectively, see figure 1. The domain along the radial direction is split into two regions with $1/2$ pipe diameter each; the first is the pipe interior where the gas-liquid mixture flows and the second encompasses the metallic pipe, the rings and the insulators. The grid size is $200 \times 200 \times 1$ volumes along the radial, axial and tangential directions with non-uniform spacing to better capture the potential gradients near the electrode borders. The grid shown in figure 1 is similar to the grid used but with fewer volumes otherwise it would not be possible to distinguish the grid lines. V is set to 2 at the

Table 1. Algebraic models for cross section void fraction, $\langle\alpha\rangle$, as a function of R^* , C^* , flow pattern and the power n representing the radial void profile.

Flow pattern	Conductive liquids	Dielectric liquids
Annular ($0.8 \leq \alpha \leq 1.0$)	$\alpha = 1 - \frac{R^*}{2.45}$	$\alpha = 0.76 + 0.31\sqrt{0.45 - C^*}$
Bubbly ($0.0 \leq \alpha \leq 0.2$)	$\alpha = g(n) (2/3) (1 - R^*)$ with $g(n) = \frac{0.129n+1.873}{0.129n+0.873}$ for $n \geq 1$	$\alpha = g(n) \left(\frac{\varepsilon_g + 2\varepsilon_l}{3\varepsilon_l} \right) (1 - C^*)$

ring electrodes and at the metallic pipe it is set to 0. Once the electrical potential field is determined, C and R are evaluated in a post-processing stage according to the surface integrals defined in equation (2).

The numerical estimates of impedance are performed for three scenarios: single phase, bubbly and annular flows. ε_m and σ_m are set according to equation (6) on the occurrence of bubbly flow, while for annular flow equation (7) is used.

A series of parametric runs is performed to obtain the impedance estimates with distinct pipe diameters and electric properties. Geometrically similar ring electrodes are used with pipe diameters spanning from 25 to 100 mm. The gas relative permittivity is set to a constant, $\varepsilon_g = 1$; the oil relative permittivity spans from 2 to 5 and the water conductivity changes from 3.5 S m^{-1} (salty water, 60 g l^{-1}) to 0.0001 S m^{-1} (deionized water).

3.3. Impedance estimate for single phase

Estimates for R or C when the sensor is filled with a gas or a liquid are obtained from numerical simulations. The data are reduced to simple algebraic expressions shown in equation (8) as a function of D , σ , ε , ε_0 and of a geometric constant K found by linear regression of the R and C data:

$$R = (\sigma KD)^{-1} \text{ and } C = \varepsilon_0 (\varepsilon_r + 10) KD, \text{ where } K = 4.9. \quad (8)$$

The constant K is dependent on the rings' geometrical properties. Therefore, its value is the same regardless of whether the fluid polarizes or conducts electrical charges. The factor 10 appearing in equation (8) applies to liquids which polarize charges because the PVC, used as an electric insulator, and the tested fluids have permittivities of the same order of magnitude. Therefore, both participate in the electrical field. The resistance is inversely proportional to the pipe diameter while the capacitance is linearly proportional to the pipe diameter. The expressions in equation (8) allow the estimation of C and R for pipes with diameters spanning from 25 to 100 mm and for fluids with distinct ε and σ including emulsions as long as the rings are geometrically similar. The fits are less than 2% off from the experimental measurements of R and C . Details of the numerical simulations and data reduction are given in Flora (2011).

3.4. Impedance estimate for two phases

The R and C estimates for annular and dispersed flows are numerically simulated for gas and liquids with various

electrical properties, pipes with distinct diameters and void fraction ranges of $0.8 \leq \langle\alpha\rangle \leq 1$ and $0 \leq \langle\alpha\rangle \leq 0.2$, respectively. These void fraction boundaries do not imply necessarily an actual flow pattern transition boundary but define the intervals where the numerical simulations were performed. The data are conveniently expressed in dimensionless form with the use of equation (9):

$$R^* = \frac{R_{\text{full}}}{R} = \frac{\sigma_l}{\sigma_m} \text{ and } C^* = \frac{C - C_{\text{void}}}{C_{\text{full}} - C_{\text{void}}} = \frac{\varepsilon_m - \varepsilon_g}{\varepsilon_l - \varepsilon_g}, \quad (9)$$

where the subscripts 'full' and 'void' mean the values that R and C have when the pipe is full of liquid ($\langle\alpha\rangle = 0$) or full of gas ($\langle\alpha\rangle = 1$). The R^* and C^* expressions are useful because they encompass the geometric factor and the electrical properties in such a way that R^* and C^* are dependent on the void fraction only, see also Andreussi *et al* (1988) and Geraets and Borst (1988). The R^* and C^* numerical data are further reduced to $\langle\alpha\rangle$ expressions, see table 1. For annular flow, $\langle\alpha\rangle$ is dependent on R^* or C^* while for bubbly flow $\langle\alpha\rangle$ also depends on the power n defining the radial void profile. The profile correction is introduced in the form of $g(n)$ as defined in table 1. $g(n)$ is greater than unity, but as the power n increases $g(n)$ approaches unity. $g = 1$ is equivalent to having a uniform radial void profile, the scenario where equation (1) applies and the numerical constants $(2/3)$ and $(\varepsilon_g + 2\varepsilon_l)/3\varepsilon_l$ appearing in the algebraic expressions for bubbly flow arise. The effect of the profile correction function, $g(n)$, is to inflate the Maxwell coefficients due to the fact that near the wall the gas concentration is lower.

The algebraic expressions in table 1 apply to geometrically similar sensors, for pipe diameters ranging from 25 to 100 mm and liquids with dielectric or conductivity constants spanning from 2 to 5 or from 3.5 to 0.0001 S m^{-1} , respectively.

3.5. Sensor's spatial sensitivity

A series of numerical runs is conducted to determine the sensor's spatial sensitivity. Figure 3 shows the rings, the insulators and the pipe wall represented along the x axis in black, white and gray colors. The x axis origin coincides with the rings' centerline and the distance from the centerline is expressed in pipe diameters. The y axis displays the relative resistance R^* as a slug of water with a cylindrical shape approaches the electrode area from the left. Initially the sensor is full of air and $R^* = 0$. The presence of the slug is felt only when its front touches the left electrode. R^* remains nearly constant until the slug front reaches the pipe wall at the right. The sensor indicates 100% full of water, i.e. $R^* = 1$, after the slug front has further advanced $0.6D$ from the right electrode. The sensor's spatial sensitivity is $1.4D$, meaning that events

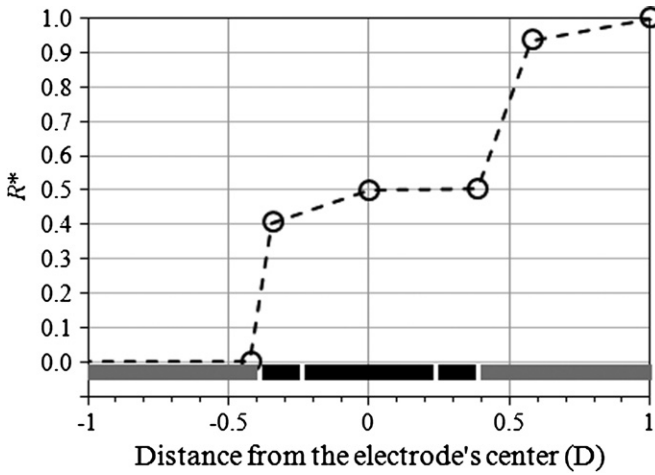


Figure 3. Spatial sensor response to the approach of a water slug in a tube initially filled with air.

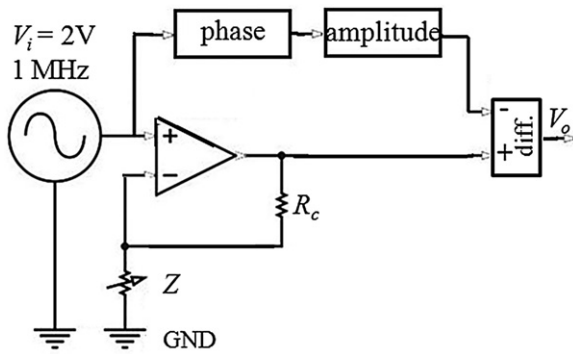


Figure 4. Circuit block diagram.

such as detecting a slug front need a pipe axial distance of $1.4D$.

4. Experimental apparatus and tests

The next sections describe the circuit driver, the experimental apparatus, the test procedures and the data set.

4.1. Electronic circuit

The sensor's driving circuit is based on a two-arm Wheatstone bridge as shown in figure 4. A 2 V and 1 MHz oscillator feeds the circuit. The choices of voltage and frequency minimize the electrode polarization effect on the electrodes and keep low power consumption. One arm of the bridge has the fluid impedance, Z , proportional to the admittance due to the operational amplifier. The wire connection to the circuit driver is shown in figure 1. The operational amplifier gain is adjusted by a charge resistor, R_c , accordingly with the medium admittance. The second arm has a circuit with adjustable phase and amplitude. The half bridge is balanced when the sensor is full of liquid. The off-balance voltages take place due to the gas content in the liquid and are measured on the differencing circuit block.

The output voltage V_o is given as a function of R_c , Z and V_i , according to equation (10):

$$V_o = V_i \left(\frac{R_c}{Z} \right). \quad (10)$$

The impedance Z is measured at ground potential. This choice allows the pipe wall to be used as the second electrode, introduces a simplification to the mechanical design and provides a shield against external electromagnetic noise.

4.1.1. The relationship of the output voltage with R^* and C^* . The relative voltage, V^* , follows the definition given in equation (9) and is expressed as

$$V^* = \frac{V_o - V_{\text{void}}}{V_{\text{full}} - V_{\text{void}}}, \quad (11)$$

where the subscripts 'full' and 'void' apply when the output voltage corresponds to a state where the pipe is full of liquid ($\alpha = 0$) or full of gas ($\alpha = 1$).

Considering a scenario where the liquid phase has a conductive behavior, i.e. $Z \equiv R$, and substituting this definition into equation (10) it is possible to rewrite equation (11) to find

$$V^* = \frac{R_c/R - R_c/R_{\text{void}}}{R_c/R_{\text{full}} - R_c/R_{\text{void}}} \equiv \frac{R_{\text{full}}}{R} \equiv R^*. \quad (12)$$

Similarly, when the liquid phase has a dielectric behavior, i.e. $Z = 1/j\omega C$, the substitution of this definition into equation (10) and equation (11) leads to

$$V^* = \frac{j\omega C R_c - j\omega C_{\text{void}} R_c}{j\omega C_{\text{full}} R_c - j\omega C_{\text{void}} R_c} \equiv \frac{C - C_{\text{void}}}{C_{\text{full}} - C_{\text{void}}} \equiv C^*. \quad (13)$$

Equations (12) and (13) are transfer functions from R^* and C^* to V^* . These functions establish a relationship between the numerically estimated quantities, R^* and C^* , and the experimentally determined voltage V^* . This property is used to compare the numerical outcome against the experimental data in the validation analysis given in section 5.

4.2. Dynamic tests

The dynamic tests consist in submitting the sensor to the instantaneous fluctuations of voids occurring in an upward co-current vertical air–water flow operating near ambient pressure and temperature. The test section is a straight vertical transparent acrylic tube, 26 mm ID and 307D long, see the schematic representation in figure 5. Air and water are injected at the lower end of the test section. The sensor, installed at 257D downstream of the mixer, is in between a pair of quick closing valves, QCV, used for void fraction measurement. The QCV are 2182 mm apart from each other and have a closing time of 12 ms. At the top end of the test section there is a U turn which discharges the mixture into a drop leg with 75 mm ID open to the atmosphere. The air is separated and discharged into the atmosphere while the water falls by gravity and returns to the storage tank. The air flow is measured using a Merian linear flow resistance meter while the water flow rate is measured using a Metroval Coriolis.

Before beginning each run the reference voltages 'full' and 'void' are set by measuring the output voltage having the pipe full of water and in sequence when it is full of

Table 2. Flow pattern identification, liquid and gas superficial velocities, void fraction measured by the QCV and the time average output voltage. Symbols: BB—dispersed bubbles, SC—spherical cap, SS—stable slug, US—unstable slug, SA—semi-annular and AA—annular flows.

Test #	Flow pattern	J_l (m s ⁻¹)	J_g (m s ⁻¹)	$\langle\alpha_{QCV}\rangle$ (—)	$\langle V^*\rangle$ (—)	Test #	Flow pattern	J_l (m s ⁻¹)	J_g (m s ⁻¹)	$\langle\alpha_{QCV}\rangle$ (—)	$\langle V^*\rangle$ (—)
1	BB	0.79	0.06	0.05	0.95	23	SS	0.60	2.40	0.64	0.54
2	BB	1.01	0.09	0.07	0.94	24	SS	0.30	0.60	0.51	0.63
3	BB	1.01	0.11	0.08	0.93	25	SS	0.60	0.60	0.43	0.72
4	BB	1.06	0.07	0.07	0.94	26	US	0.30	2.60	0.73	0.48
5	BB	1.19	0.04	0.04	0.97	27	US	0.40	4.20	0.78	0.49
6	BB	1.21	0.07	0.06	0.95	28	SA	0.30	6.70	0.81	0.45
7	BB	1.20	0.10	0.07	0.93	29	SS	1.20	0.56	0.24	0.80
8	BB	1.18	0.15	0.10	0.91	30	SS	0.60	0.27	0.25	0.80
9	BB	1.19	0.18	0.11	0.91	31	SS	0.92	0.53	0.30	0.76
10	BB	1.39	0.03	0.03	0.98	32	SS	1.20	0.82	0.34	0.74
11	BB	1.40	0.07	0.06	0.95	33	SS	0.30	0.28	0.34	0.73
12	BB	1.40	0.18	0.11	0.90	34	SS	0.61	0.55	0.38	0.71
13	BB	1.40	0.23	0.13	0.89	35	SS	1.21	1.07	0.39	0.71
14	BB	1.40	0.26	0.14	0.88	36	SS	0.90	0.82	0.41	0.69
15	BB	1.40	0.31	0.15	0.87	37	AA	0.35	17.90	0.87	0.29
16	BB	1.43	0.34	0.16	0.87	38	AA	1.24	17.60	0.86	0.30
17	BB	1.20	0.20	0.09	0.93	39	AA	0.92	26.55	0.90	0.25
18	SC	0.30	0.10	0.13	0.88	40	AA	0.64	17.15	0.87	0.30
19	SC	0.60	0.20	0.18	0.83	41	AA	0.35	18.60	0.87	0.30
20	SS	0.40	1.00	0.56	0.57	42	AA	0.28	26.43	0.92	0.19
21	SS	0.60	1.00	0.49	0.63	43	AA	0.32	29.32	0.92	0.20
22	SS	0.40	1.50	0.61	0.54	44	AA	0.67	28.60	0.89	0.23

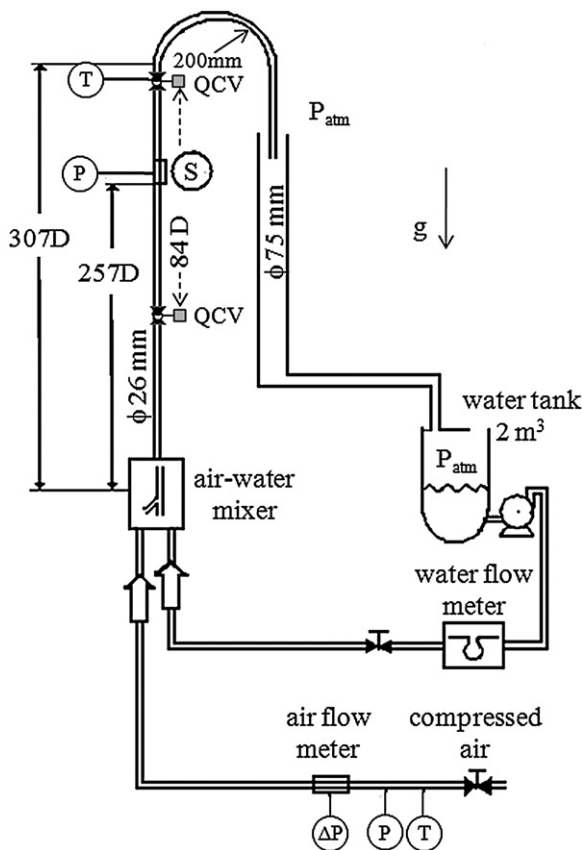


Figure 5. Air–water vertical test section.

air. Each test consists in setting the air and water flow rates, waiting for the flow rate to stabilize and then acquiring the output voltage during 60 s at a rate of 3000 samples per

second. After finishing the data acquisition the pair of QCV is activated to measure the average void fraction. When closed, the valves trap a volume of mixture allowing direct observation of fractions of air and water due to the air–water segregation (Elkow and Rezkallah 1996, Costigan and Whalley 1996). After storing the void fraction values the valves are re-opened and the procedure is repeated for another 3 to 5 times to ensure good data representation. Table 2 shows the test grid with 44 experimental data points identifying the flow pattern, the superficial velocities J_l and J_g , the void fraction measured by the QCV $\langle\alpha_{QCV}\rangle$ and the time average voltage $\langle V^*\rangle$. In order to get an accurate description of the spatial void distributions the flow pattern descriptors include the transitional boundaries as well as internal classifications (Rosa *et al* 2010). The symbol BB represents the disperse bubble flow. The symbols SS and US denote stable and unstable slug, also known as an internal classification of the intermittent flow pattern. The symbols SC and SA stand for spherical cap and semi-annular. They are known as the transitional flow patterns from bubble to intermittent flow and from intermittent to annular pattern, respectively. For referencing purpose visual identification of each flow pattern is shown in figure 6.

The experimental data span from bubbly to annular flows and their representativeness is better seen on the flow map of Taitel *et al* (1980) shown in figure 7. The map displays boundaries for bubbly, intermittent and annular patterns. Here it is considered that the intermittent pattern encompasses the SC, SS, US and SA flow patterns. Additionally the map also displays figures, next to the open symbols, indicating the measured void fraction as a reference. The void fraction data displayed on the map follow the expected trend; they increase as J_g increases for a constant J_l . It is also possible to observe the transitions from bubbly to intermittent flow and intermittent to

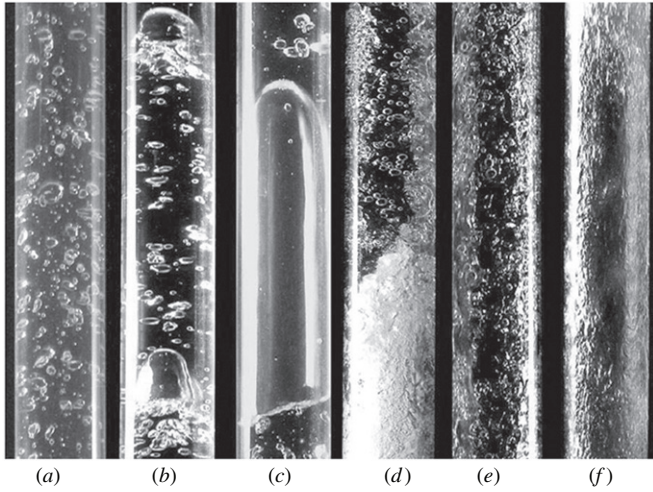


Figure 6. Test section photographs of upward air–water flow exhibiting the visual flow pattern features: (a) bubbly—BB; (b) spherical cap—SC; (c) stable slug—SS; (d) unstable slug—US; (e) semi-annular—SA and (f) annular—AA.

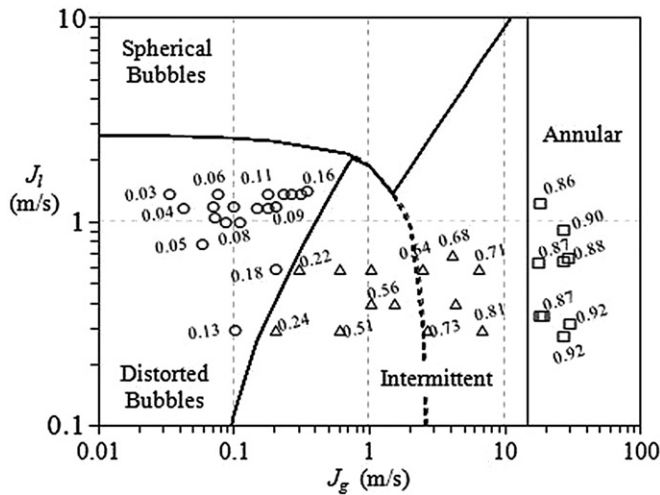


Figure 7. Flow map identifying the bubbly, intermittent and annular flow patterns. Symbols: \circ bubbly, Δ intermittent and \square annular. The transitional boundaries are defined by Taitel's map. The numbers close to the symbols represent the experimental void fraction.

annular flow occurring for void fractions around 0.2 and 0.85, respectively.

The uncertainty estimate for $\langle \alpha_{QCV} \rangle$ is ± 0.015 due to the measurement of the trapped volume, the number of samples taken and the QCV closing interval. Similarly, the uncertainty estimate for $\langle V^* \rangle$ is ± 0.010 due to the measurement of the voltages related to the 'full' and 'void' states and to the oscillations in temperature and ion concentration.

5. Analysis

This section analyses the accuracy and the validity of the impedance models for bubbly and annular flow patterns and proposes an extension to apply to the intermittent flow pattern. Since the input parameter is the instantaneous value of V^* and

the model's accuracy is tested against the averaged values of $\langle \alpha_{QCV} \rangle$ it is convenient to define the average procedures and the absolute errors before proceeding to the analysis.

The instantaneous signal of V^* is flow pattern-dependent and fluctuates around the average. Figure 8 displays the time series of V^* and its probability density function (PDF) for selected points spanning from bubbly to annular flow with increasing gas velocity. The bubbly flow has its V^* in a narrow distribution close to unity due to the high liquid content of the mixture. As the gas velocity increases V^* exhibits peaks near 0.5, characteristic of the spherical caps formation. Additional increment in the gas flow leads to stable slug and unstable slugs with V^* values alternating within 0.8 and 0.3 approximately corresponding to the intermittent passage of the aerated liquid pistons and elongated bubbles. Further increase in the gas causes the semi-annular and the annular flows displacing the distributions to the left with most probable values around 0.4 and 0.15, respectively.

The algebraic expressions for annular and bubbly flows given in table 1 can be expressed as a function of V^* , the instantaneous readout, considering the transfer functions defined in equations (12) and (13). The average void fraction, $\langle \alpha \rangle$, is obtained in three steps.

- (1) The time series of the output voltage is transformed into the relative voltage, V^* , applying the measured reference values V_{full} and V_{void} as given in equation (11).
- (2) The relative voltage V^* time series is transformed into the void fraction time series by applying the equations in table 1.
- (3) The void fraction time series is averaged to obtain the mean void fraction, $\langle \alpha \rangle$.

The model accuracy is gauged by comparing the estimates against experimental data. For this purpose, the following definitions of absolute error and its root mean squared value are used:

$$\delta = \langle \alpha_{QCV} \rangle - \langle \alpha \rangle \text{ and } \delta_{RMS} = \sqrt{\frac{1}{N} \sum_{i=1}^N (\langle \alpha_{QCV} \rangle - \langle \alpha \rangle)^2}. \quad (14)$$

5.1. Annular flow and bubbly flow data comparison

The set equations given in table 1 hold until the annular or the bubbly flow patterns happen. Inserting the air–water electrical properties into the equations one obtains the algebraic expressions given in equation (16) for reference. The equations' accuracy is assessed by comparing the estimates of $\langle \alpha \rangle$ against the experimental data of $\langle \alpha_{QCV} \rangle$ given in table 2. The data comparison is shown in figure 9 for annular and bubbly flow patterns. The open symbols represent the experimental data with the associated error bars while the lines are the algebraic expressions. The dependence of the void fraction estimate for bubbly flows on the radial void profile is shown in figure 9(b) for powers of n of 2, 3 and 4 and also for the uniform profile. It is observed that the model employing the uniform radial void profile does not follow the experimental data trend but the use of radial void profiles with

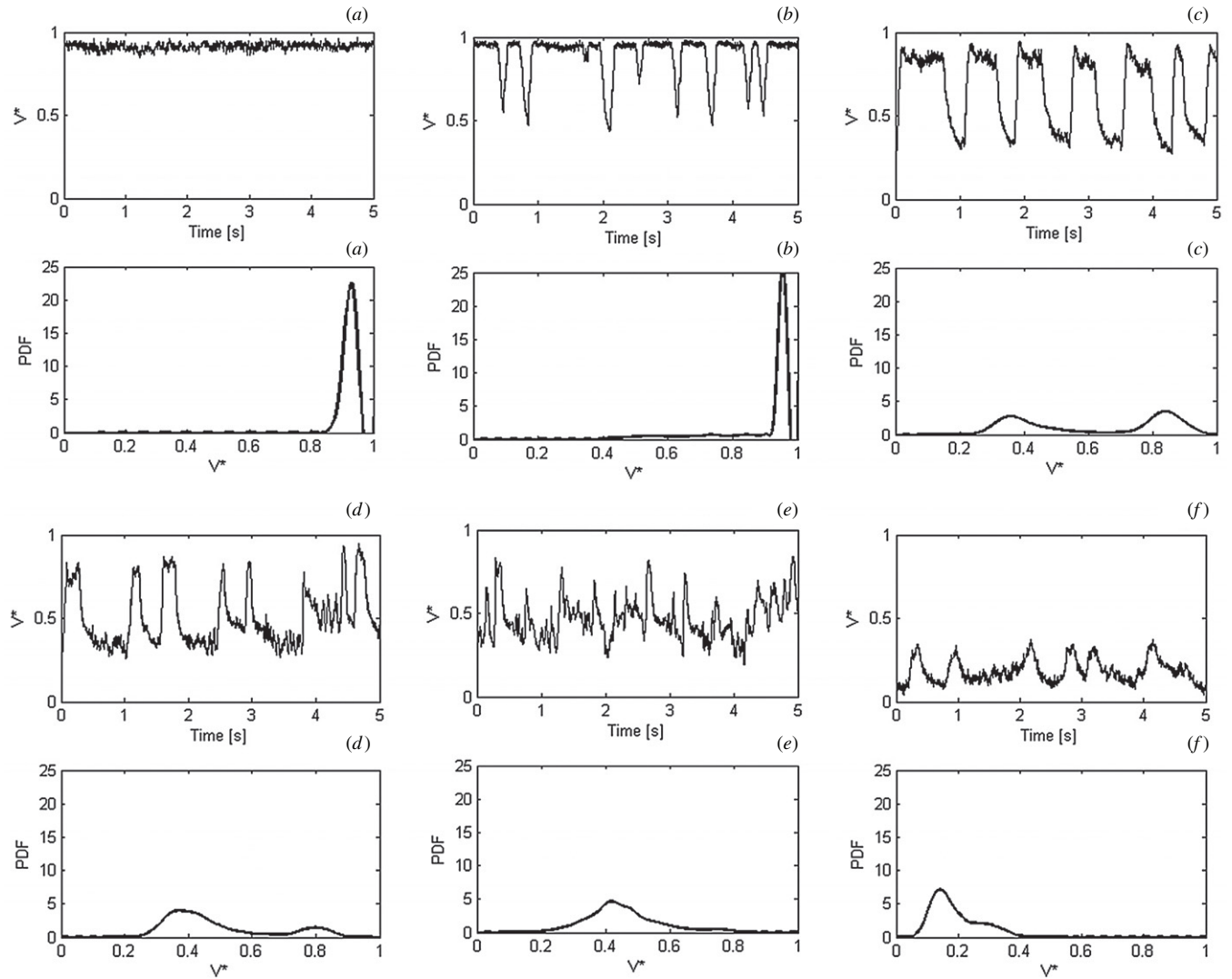


Figure 8. Relative voltage, V^* : temporal signal and its PDF with increasing air velocities for selected data points. (a) bubbly #8; (b) spherical cap #18; (c) stable slug #24; (d) unstable slug #26; (e) semi-annular #28 and (f) annular #42.

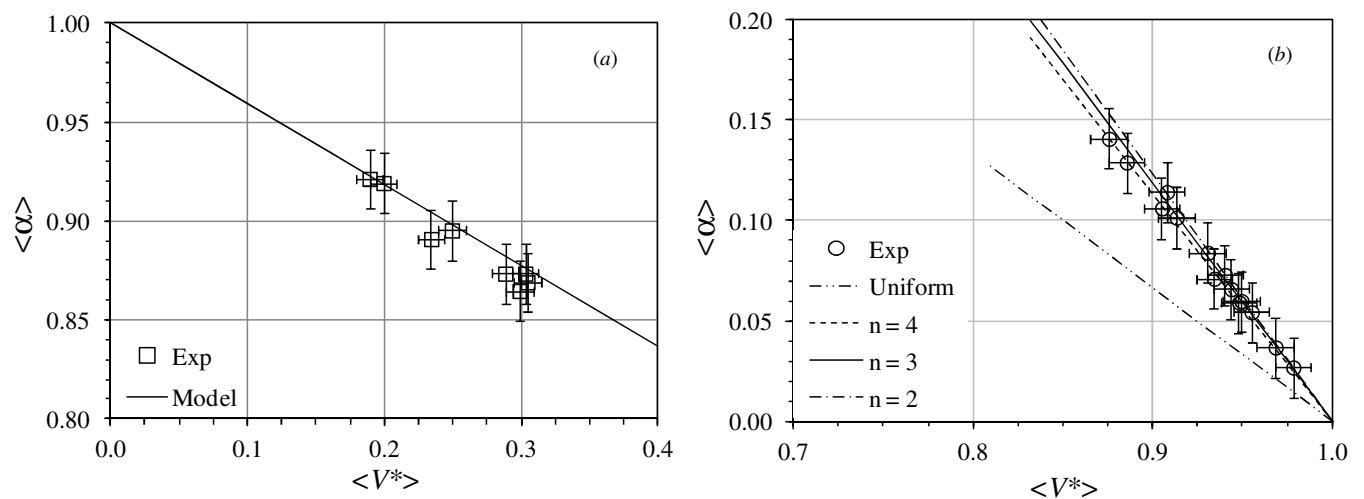


Figure 9. Predicted and experimental values of the cross section void fraction and error bars. (a) Annular flow and (b) bubbly flow for uniform radial void profile and power profiles with $2 \leq n \leq 4$.

Table 3. Absolute error comparison between the model and a polynomial fit from the experimental data.

		Flow pattern			
		Bubbly	Intermittent	Annular	Overall
Model	Max. abs. error	0.008	0.023	0.014	0.023
	Min. abs. error	−0.004	−0.092	−0.001	−0.092
	RMS abs. error	0.004	0.030	0.008	0.021
Exp. fit	Max. abs. error	0.017	0.042	0.018	0.042
	Min. abs. error	−0.014	−0.067	0.000	−0.067
	RMS abs. error	0.008	0.026	0.009	0.019

the Maxwell model does capture experimental data. The radial void profile with n of 3 has the minimum RMS error of 0.008. The application of the Maxwell model without considering the radial void profile leads to a RMS error of 0.1849. This work recommends the use of $n = 3$ for numerical evaluation purposes on bubbly flows exhibiting core-peak radial void profiles.

Table 3 shows the maximum and the minimum absolute errors as well as the RMS error for annular and bubbly flow patterns of 0.014, −0.001, 0.008 and 0.008, −0.004 and 0.004, respectively. These figures ensure the success of the mathematical modeling of the impedance for annular and bubbly flow patterns within the uncertainty of the experimental data.

The validity of the analytical expressions given in table 1 still lacks a domain definition of V^* where the annular and bubbly flows occur. The V^* boundaries can be defined considering first the transition boundaries in terms of α and then, employing the inverse function, one obtains the V^* boundaries.

The transition between bubbly and intermittent flow roughly occurs for $0.20 \leq \alpha \leq 0.25$ (Taitel *et al* 1980); therefore a threshold value of $\alpha = 0.20$ as an upper bound for the bubbly flow is proposed. The transition to annular flow is not defined in terms of α but as a function of a velocity capable of carrying over a droplet (Taitel *et al* 1980). This transitional criterion does not have a straightforward application to the present case. Instead, the use of a threshold value of $\alpha = 0.85$ as a lower bound for the annular pattern is proposed. This threshold estimate is based on experimental readings of void fraction displayed on the flow map in figure 7 at the annular transition boundary. Employing the threshold values it is possible to define a range of α for bubbly and annular flows as $0.00 \leq \alpha \leq 0.20$ and $0.85 \leq \alpha \leq 1.00$, respectively. Applying the extreme values of each flow pattern range into the impedance models for air–water flows, or else in figure 9, one finds the corresponding intervals for V^* of $0 \leq V^* \leq 0.37$ and $0.83 \leq V^* \leq 1.00$.

The domain boundaries for V^* have theoretical support for bubbly flow and experimental evidence for annular flow but they may not necessarily define an accurate transition boundary among flow patterns. In fact they are used as reference values to estimate void fraction. The approximate nature of the domain boundaries for V^* is justified considering that $\langle \alpha \rangle$ changes continuously, not in jumps, along flow pattern transitions as observed in figure 7. This means that the neighboring values of V^* outside the domain boundaries

are still good approximations because $\langle \alpha \rangle$ does not have discontinuities.

5.2. Intermittent flow

The annular and bubbly flows define the lower and upper ranges of V^* . For air–water flow these ranges were defined in the previous section and a gap is observed in the interval $0.37 < V^* < 0.83$ where there is no model to map α to V^* . This gap encompasses the intermittent flow which lies between annular and bubbly flows. For reference figure 8 displays for selected data points how V^* is distributed on the sub-regimes which form the intermittent flow.

A polynomial fit encompassing the entire range of experimental data discloses the gap as a bridge region whose ends merge into the annular and bubbly flow models. This behavior is seen in figure 10(a) employing a fourth degree polynomial fit:

$$\alpha = 3.181(V^*)^4 - 5.422(V^*)^3 + 1.795(V^*)^2 - 0.553(V^*) + 1. \quad (15)$$

The accuracy of the polynomial fit is shown in table 3 for bubbly, intermittent and annular flows separately and the last column shows the figures encompassing all flow patterns. As a reference the RMS error over the whole data set is 0.019.

The impedance model of the intermittent flow follows the polynomial behavior. It links the ends of the impedance models with a straight line as suggested in figure 10(b) where the continuous lines represent the impedance models of the annular and bubbly flows, the dotted lines are extrapolation trends and the dashed line is the impedance model of the intermittent flow linking the ends of the models. For air–water flows the model consists of a linear interpolation fit joining the coordinates (0.85, 0.37) to (0.20, 0.83), the first and second elements being the pair (α, V^*) which have their values previously defined in the last section. For completeness the set of algebraic equations for α estimate and the associated V^* intervals are given in equation (16):

$$\alpha = \begin{cases} 1 - (V^*/2.45) & \text{if } 0.00 \leq V^* \leq 0.37 \\ \rightarrow \text{annular flow} \\ 1.41(1 - V^*) - 0.04 & \text{if } 0.37 < V^* < 0.83 \\ \rightarrow \text{intermittent flow} \\ 1.19(1 - V^*) & \text{if } 0.83 \leq V^* \leq 1.00 \rightarrow \text{bubbly flow.} \end{cases} \quad (16)$$

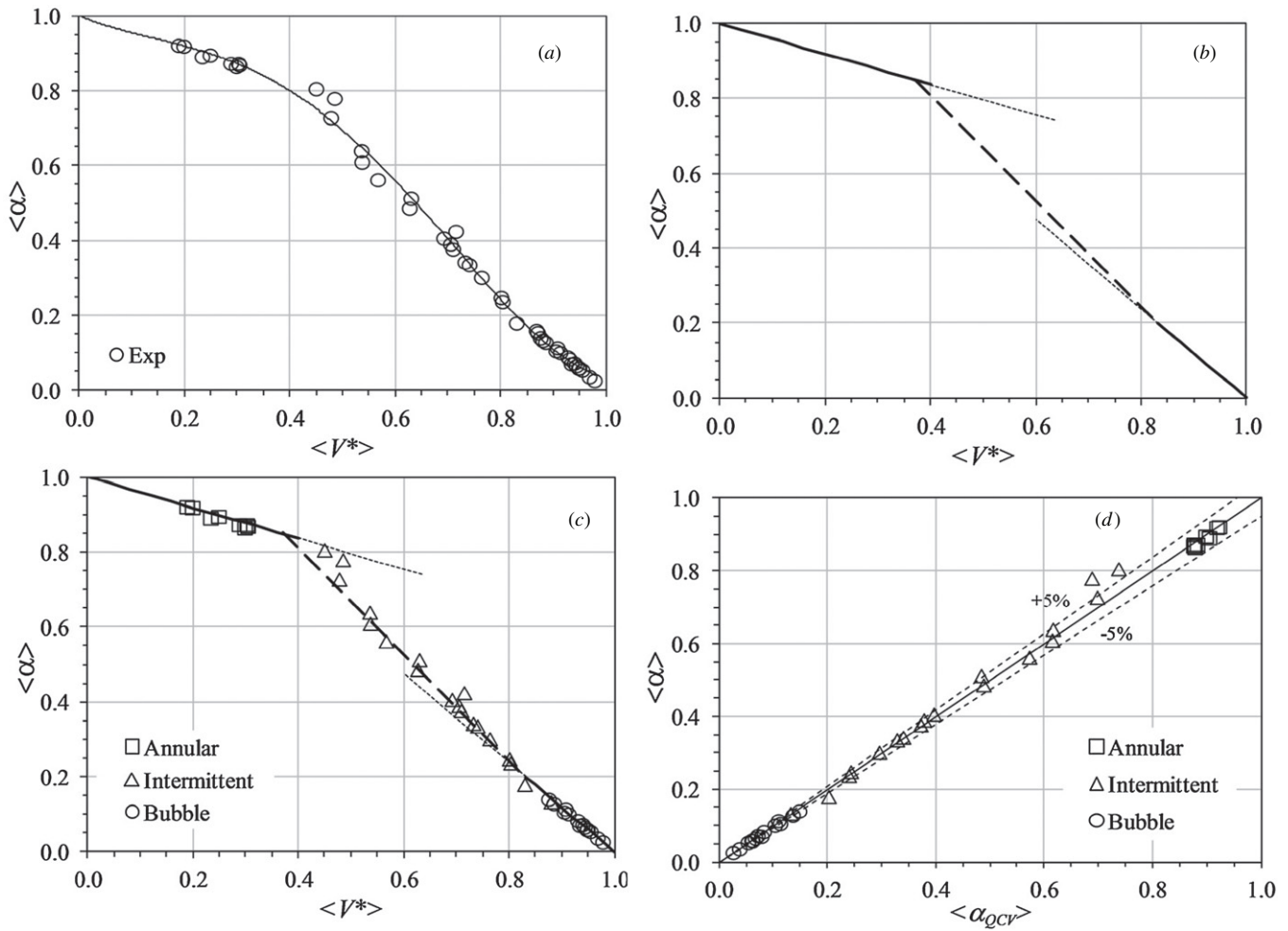


Figure 10. Predicted and experimental values of the cross section void fraction for the annular, intermittent and bubbly flow patterns. (a) Polynomial fit of the experimental data; (b) proposed fit, linear by parts; (c) proposed fit and experimental data superposed and (d) predicted and measured average void fraction.

Equation (16) shows a linear-by-parts model derived through the numerical method. The void fraction always decreases with V^* but the sensor's sensitivity, $d\alpha/dV^*$, changes with the flow pattern. For bubbly, intermittent and annular flows one finds $d\alpha/dV^*$ of -1.19 , -1.41 and -0.41 , respectively. The growth rate is better seen in figure 10(c) which also compares the experimental data trend against the model prediction represented by straight lines. Lastly, the predicted versus measured $\langle \alpha \rangle$ is shown in figure 10(d) with error bounds of $\pm 5\%$. It is observed that most of the estimates fall within this interval; the exceptions are the #27 and #28 data points which are better represented by the annular fit instead. These points are like transitional points which the linear-by-parts model does not map accurately.

The model and the experimental data fit have their errors compared in table 3 for each flow pattern separately and also covering all data sets. The model has a better accuracy in regard to the polynomial fit on the bubbly and annular flow patterns but it is surpassed by the polynomial fit on the intermittent pattern. This behavior is expected since $\langle \alpha \rangle$ estimates for bubbly and annular flows have models based on the physics of the flow which, by first principles, must have a superior performance. On the other hand for the intermittent flow the

$\langle \alpha \rangle$ estimates are based on a straight line fit which is expected not to be accurate at the transitional regions. Despite these qualitative observations the differences between fits are small if one looks at the model and experimental fit RMS errors of 0.021 and 0.019 in relation to an experimental data uncertainty of ± 0.015 . Considering the error analysis it is possible to conclude that the hypothesis to model $\langle \alpha \rangle \times V^*$ by a straight line fit joining the boundaries of the annular and bubbly flows is a good approximation.

5.3. Void fraction distributions

A short exploration of the flow pattern influence on the instantaneous void fraction and its associated PDF is developed to support the model reliability. In fact, the use of the void fraction as an objective flow pattern indicator is explored in several works; a review on the subject is in Rosa *et al* (2010). Figure 11 shows the instantaneous void fractions and their PDF in a succession of flow patterns which occur when the gas velocity increases from 0.1 to 26 m s⁻¹. The changes in the shape of the temporal signal or its PDF are due to the changes in the spatial distribution of voids inside the pipe. This short analysis focuses on the PDF which brings the α variability

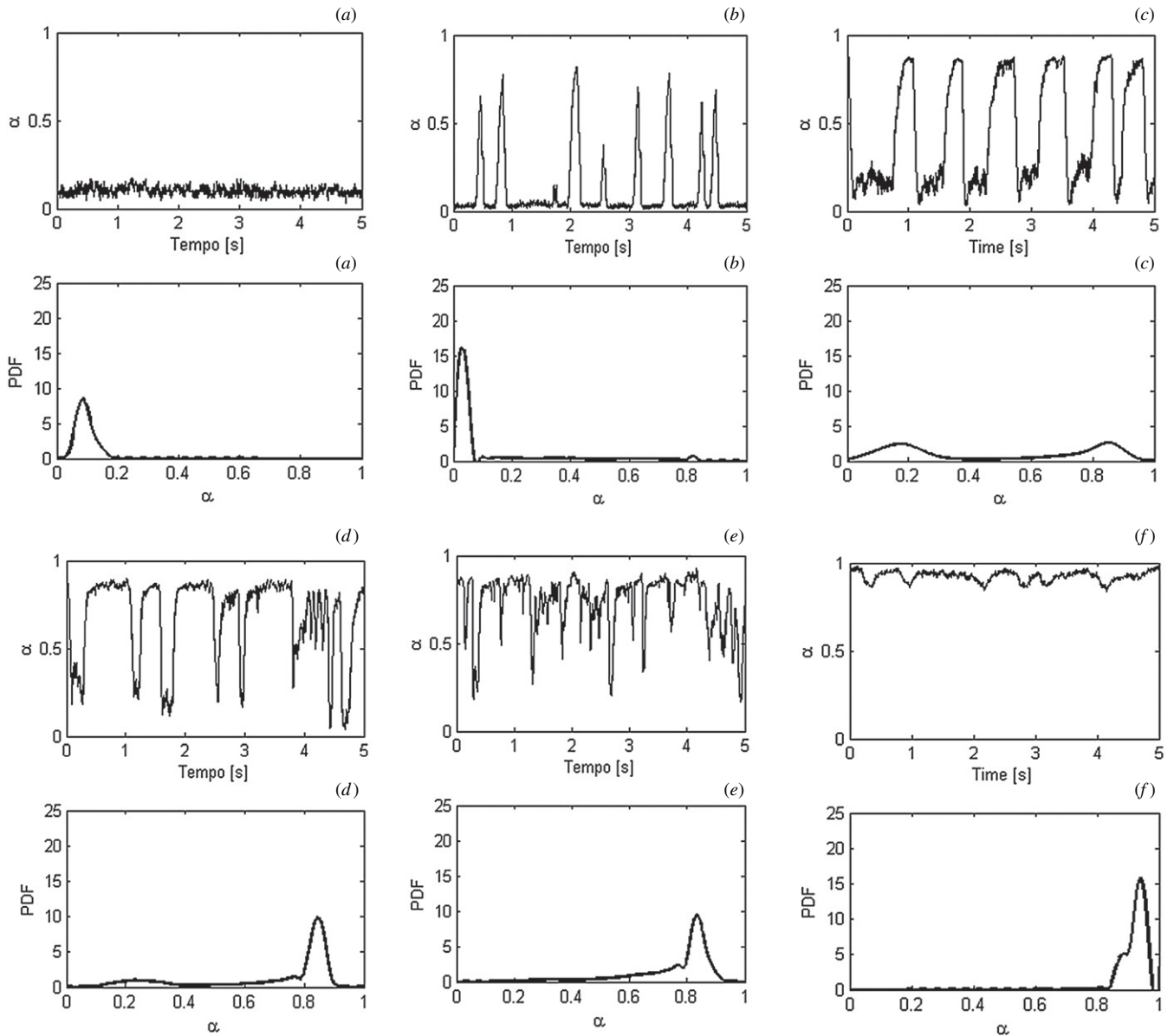


Figure 11. Void fraction temporal signals and its PDF with increasing air velocities. (a) Bubbly #8; (b) spherical cap #18; (c) stable slug #24; (d) unstable slug #26; (e) semi-annular #28 and (f) annular #42 flow patterns.

and its most probable value. The bubbly flow, figure 11(a), has a symmetrical distribution and a most probable value of α of 0.10. The spherical cap flow pattern, figure 11(b), still has low α values but shows peaks of 0.5 indicating the passage of spherical caps; it has a non-symmetrical distribution skewed toward the right and its most probable value is $\alpha \approx 0.10$. The stable and the unstable slugs, figures 11(c), (d), have bimodal distributions due to the intermittence. Figure 11(e) shows the semi-annular flow, a transitional pattern between the intermittent and annular flow, and has its distribution skewed toward the left with its most probable value of $\alpha \approx 0.8$. As the gas flow rate increases, the population of low α values existing on the semi-annular flow disappears, the void fraction values range from 0.8 to 0.95 and the annular pattern is achieved, see figure 11(f), with the distribution slightly skewed toward the left.

6. Conclusions

The favorable comparison against experimental data supports the usefulness of the numerical method as a design tool as well as a procedure to obtain the sensor's calibration curve. It is possible to establish the void meter calibration curve based on numerical modeling of the flow impedance. This work introduces a novel technique, based on the Maxwell model, to estimate the electrical impedance in bubbly flows taking into account the radial void profile. The developed impedance models apply to bubbly and annular flows; the impedance model of the intermittent flow comes from an interpolation between these two flow patterns. The void fraction estimates are compared against experimental data taken on air–water flow and exhibited a RMS error of 0.021 for an experimental data uncertainty of ± 0.015 .

The work introduces the use of multiple ring electrode geometry, explores the use of electrical impedance similarity and proposes the measurement of Z with a fixed reference, the ground. The multiple ring electrodes enhance the sensor's void fraction sensitivity near the pipe as well as at the pipe core. The use of geometrical similarity extends the validity of the impedance models to pipes of different diameters. Employing the ground as reference to the impedance measurement allows the metallic pipe to be used as the receiving electrode, and provides a shield against electromagnetic and electrostatic external sources.

During this first stage of sensor's development several issues were considered out of scope. This paragraph is an attempt to acknowledge a few of them. The void meter lacks an absolute reference to the states 'full' and 'void'. Future developments will focus on the self-referencing routines. For oil field applications, among other aspects, the development of digital electronics for remote communication, field tests, the addressing of safety issues concerning the operation in risk areas and power consumption are still necessary.

Acknowledgments

The authors gratefully acknowledge the research grant from Petrobras under contract no 00500029781.07.2; also B F Flora thanks CAPES for a scholarship from 2009 to 2011.

References

- Abouelwafa M S A and Kendall E J M 1980 The use of capacitance sensors for phase percentage determination in multiphase pipelines *IEEE Trans. Instrum. Meas.* **29** 24–7
- Ahmed W H 2006 Capacitance sensors for void-fraction measurements and flow-pattern identification in air–oil two-phase flow *IEEE Sensors J.* **6** 1153–63
- Andreussi P, Donfrancesco A and Messina M 1988 An impedance method for the measurement of liquid hold-up in two-phase flow *Int. J. Multiph. Flow* **14** 777–85
- Asali J C, Hanratty T J and Andreussi P 1985 Interfacial drag and film height for vertical annular flow *AIChE J.* **31** 895–902
- Brennen C E 2005 *Fundamentals of Multiphase Flow* (Cambridge: Cambridge University Press)
- Carnière H, Joen C T, Willockx A, Paepe M, Christians M, Rooyen E, Liebenberg L and Meyer J P 2007 Horizontal two-phase flow characterization for small diameter tubes with a capacitance sensor *Meas. Sci. Technol.* **18** 2898–909
- Ceccio S L and George D L 1996 A review of electrical impedance techniques for the measurement of multiphase flows *J. Fluids Eng.* **118** 391–9
- Cimorelli L and Evangelisti R 1967 The application of the capacitance method for void fraction measurement in bulk boiling conditions *Int. J. Heat Mass Transfer* **10** 277–88
- Coney M W E 1973 The theory and application of conductance probes for the measurement of liquid film thickness in two phase flow *J. Phys. E: Sci. Instrum.* **6** 903–10
- Costigan C and Whalley P B 1996 Slug flow regime identification from dynamic void fraction measurements in vertical air–water flows *Int. J. Multiph. Flow* **23** 263–82
- Elkow K J and Rezkallah K S 1996 Void fraction measurements in gas–liquid flows under 1–g and μ -g conditions using capacitance sensors *Int. J. Multiph. Flow* **23** 815–29
- Flora B F 2011 Ring impedance sensor for void fraction measurement in gas–liquid flows *MSc Dissertation* State University of Campinas, Brazil
- Fossa M, Guglielmini G and Marchitto A 2003 Intermittent flow parameters from void fraction analysis *Flow Meas. Instrum.* **14** 161–8
- Geraets J J and Borst J C 1988 A capacitance sensor for two-phase void fraction measurement and flow pattern identification *Int. J. Multiph. Flow* **14** 305–20
- Gregory G A and Mattar L 1973 An *in-situ* volume fraction sensor for two-phase flows of non-electrolytes *J. Can. Pet. Technol.* **12** 48–52
- Guet S and Ooms G 2006 Fluid mechanical aspects of gas lift technique *Ann. Rev. Fluid Mech.* **38** 225–49
- Hammer E A, Dyakowski T and Johansen G A 2006 *Multiphase Flow Handbook* ed C T Crowe (Boca Raton, FL: CRC Press)
- Haus H A, Melcher J R, Zahn M and Silva M L 1989 *Electromagnetic Fields and Energy* (Englewood Cliffs, NJ: Prentice Hall)
- Hibiki T and Ishii M 2002 Distribution parameter and drift velocity of drift-flux model in bubbly flow *Int. J. Heat Mass Transfer* **45** 707–21
- Kim S, Lee J S, Kim K Y, Kang K H and Yun B J 2010 An approximate formula for the capacitance–void fraction relationship for annular flows *Meas. Sci. Technol.* **20** 125404
- Liu T J 1993 Bubble size and entrance length effects on void development in a vertical channel *Int. J. Multiph. Flow* **19** 99–113
- Lowe D and Rezkallah K S 1999 A capacitance sensor for the characterization of microgravity two-phase liquid-gas flows *Meas. Sci. Technol.* **10** 965–75
- Maxwell J C 1873 *A Treatise on Electricity and Magnetism* (Oxford: Oxford University Press)
- Merilo M, Dechene R L and Cichowlas W M 1977 Void fraction measurement with a rotating electric field conductance gauge *Trans. ASME J. Heat Transfer* **99** 330–3
- Rocha M S and Simões-Moreira J R 2008 Void fraction measurement and signal analysis from multiple-electrode impedance sensors *Heat Transfer Eng.* **29** 924–35
- Rosa E S, Salgado R M, Ohishi T and Mastelari N 2010 Performance comparison of artificial neural networks and expert systems applied to flow pattern identification in vertical ascendant gas liquid flows *Int. J. Multiph. Flow* **36** 738–54
- Sami M, Abouelwafa A and Kendall E J M 1980 The use of capacitance sensors for phase percentage determination in multiphase pipelines *IEEE Trans. Instrum. Meas.* **29** 24–7
- Serizawa K, Kataoka I and Michiyoshi I 1975 Turbulence structure of air–water bubbly flow: I. Measuring techniques *Int. J. Multiph. Flow* **2** 221–33
- Sowa J M, Sheng P, Zhou M Y, Chen T, Serres A J and Sieben M C 1995 Electrical properties of bitumen emulsions *Fuel* **74** 1176–9
- Taitel Y, Barnea D and Dukler A E 1980 Modelling flow pattern transitions for steady upward gas–liquid flow in vertical tubes *AIChE J.* **26** 345–54
- Tsochatzidis N A, Karapantios T D, Kostoglou M V and Karabelas A J 1992 A conductance method for measuring liquid fraction in pipes and packed beds *Int. J. Multiph. Flow* **5** 653–67